Research paper

Fast automated airborne electromagnetic data interpretation using parallelized particle swarm optimization

Jacques K. Desmarais [a,b,*], Raymond J. Spiteri [c]

[a] Geological Sciences, University of Saskatchewan, 114 Science Place, Saskatoon, Saskatchewan, S7N 5E2, Canada
[b] Dipartimento di Chimica, Università di Torino, Via Giuria, 5, 10125, Torino, Italy
[c] Computer Sciences, University of Saskatchewan, 110 Science Place, Saskatoon, Saskatchewan, S7N 5C9, Canada

A B S T R A C T

A parallelized implementation of the particle swarm optimization algorithm is developed. We use the optimization procedure to speed up a previously published algorithm for airborne electromagnetic data interpretation. This algorithm is the only parametrized automated procedure for extracting the three-dimensionally varying geometrical parameters of conductors embedded in a resistive environment, such as igneous and metamorphic terranes. When compared to the original algorithm, the new optimization procedure is faster by two orders of magnitude (factor of 100). Synthetic model tests show that for the chosen system architecture and objective function, the particle swarm optimization approach depends very weakly on the rate of communication of the processors. Optimal wall-clock times are obtained using three processors. The increased performance means that the algorithm can now easily be used for fast routine interpretation of airborne electromagnetic surveys consisting of several anomalies, as is displayed by a test on MEGATEM field data collected at the Chibougamau site, Québec.

1. Introduction

The interpretation of airborne electromagnetic (AEM) data is hampered by complex survey and target configurations (Smith and Chouteau, 2006). As a result, manual interpretation of entire AEM surveys is difficult, if not infeasible. The interpretation can be simplified using algorithmic procedures. Here, we classify such procedures into two categories: inversion schemes and automated interpretation algorithms (AIA). The advantage of inversion schemes is that (in principle) no approximations need to be made about the nature of the conductivity model, so that Maxwell's equations are essentially solved exactly for the conductivity structure of the Earth. The disadvantage of inversion schemes is the non-uniqueness of the solutions; hence we refer to them as non-automated. A recent review of AEM inversion schemes is given by (Yin et al., 2015). In contrast to inversion schemes, AIAs make assumptions about the nature of the conductivity model but result in unique solutions.

Along with similar layered earth inversions (LEIs), by far the most commonly used AIAs today are the conductivity depth imaging (CDI) methods, in which it is assumed that the Earth consists of a series of horizontal layers. The procedure for CDI consists of transforming the electromagnetic data into a plot of conductivity as a function of pseudo-depth (Macnae et al., 1991). Although this approach may work well in certain situations, such as stratified sedimentary basins, CDIs (and LEIs)

may yield erroneous results if the Earth is not approximated well by layers (Wolfgram et al., 1998; Reid et al., 2010). Hence, there is a need for alternatives to the CDIs (and LEIs). Of particular interest to mineral exploration and geological mapping is the situation of large igneous and metamorphic terranes, such as the Canadian Shield, in which the Earth is resistive and usually not layered. In such cases, the use of free-space discrete conductor modeling is common practice (Dyck et al., 1981; Dyck and West, 1984; Lamontagne et al., 1988; Macnae et al., 1998; Schaa, 2010; Smith and Wasylechko, 2012; Macnae, 2015; Vallée, 2015; Fullagar et al., 2015; Desmarais and Smith, 2015a, 2015c, 2015d, 2016).

An AIA for interpretation of AEM data in resistive environments was presented by Desmarais and Smith (2015b). To the authors' knowledge, this algorithm is the only parameterized AIA that can be used to recover the three-dimensionally varying geometrical parameters of discrete targets embedded in a resistive environment. The method was shown to be highly successful as displayed by thousands of synthetic examples and two field examples. Desmarais and Smith (2015d) used a modified version of the algorithm of Desmarais and Smith (2015b) to design a multi-component-transmitter-receiver system capable of recovering the geometrical parameters of axially symmetric targets. One weakness of the algorithm of Desmarais and Smith (2015b) is the inefficient minimization of the misfit function through direct sampling of the parameter space on a uniform grid.

AEM surveys often collect data on hundreds of anomalies, so that

---

AIAs need to be highly efficient for routine interpretation. Here, we investigate alternative approaches for minimizing the misfit function of Desmarais and Smith (2015b) in order to improve the performance of the code. To this end, we make use of parallel computing tools because these are becoming commonplace in electromagnetic data interpretation (see Pethick and Harris, 2016 and references therein). In particular, we choose to implement a parallelized version of the Particle Swarm Optimization (PSO) method, originally proposed in Kennedy and Eberhart (1995). There are two main contributions arising from this paper. First is the development and performance analysis of a new, more sophisticated parallelization technique for PSO, and second is the implementation of this parallelized PSO technique as a method that can quickly and automatically interpret large AEM surveys.

The PSO method is a global optimization method that has gained popularity in the search for solutions to inverse geophysical problems (Reddy and Kumar, 2005; Fernández-Álvarez et al., 2006; Shaw and Srivastava, 2007; Fernández-Martínez et al., 2008, 2010; Naudet et al., 2008; Fernández-Martínez et al., 2010; Cheng et al., 2015). An advantage of PSO is that it is a derivative-free global optimization method; i.e., it does not require the evaluation of gradients of the objective function. This is particularly beneficial for our purposes because the objective function of Desmarais and Smith (2015b) contains a generalized inverse (Penrose, 1955). We prefer to avoid the explicit evaluation of the gradient of the generalized inverse because it is a numerically challenging procedure (Golub and Pereyra, 1973). In the context of derivative-free optimization methods, the PSO approach is especially attractive because it makes few assumptions about the problem being optimized; performance is governed through adjustment of a few empirical parameters. Here, we adopt the standard PSO algorithm for optimization of the objective function. Other PSO variants, such as the continuous linear PSO, generalized PSO, centered PSO, centered progressive PSO methods, etc., have been proposed, each of which are characterized by different stability regions and convergence rates (Fernandez-Martinez and Garcia-Gonzalo, 2009, 2011; Pallero et al., 2015). These methods have been shown to be successful in solving geophysical inverse problems (e.g., Fernández-Martínez et al., 2010). However, we obtain satisfactory results and performance using the standard approach. This is in agreement with the results of Voss (2016), where it was found that the standard PSO was superior to a number PSO variants in terms of efficiency on a large selection of test problems. We therefore limit our study to the standard PSO method.

2. Methods

2.1. Objective function

Our model attempts to describe observed AEM measurements along flight lines. Along the lines proposed in Desmarais and Smith (2015b), we develop a model using a dipole approximation. The parameters of the dipole are determined using an inversion procedure, in which the objective function plays a key role. For our model, the objective function is defined to have a magnitude that reflects the goodness-of-fit in terms of the least-squares difference between the measured and calculated data. Our goal is to minimize this objective function I with respect to the geometrical parameters (strike, dip, depth, position along the traverse line, and transverse to the traverse line) of the dipole (see Fig. 1) (Desmarais and Smith, 2015b):

$$I = -\prod_{j=x,y,z} \left[1 - \frac{\sum_{i=1}^{q} \left(\mathscr{R}_{j,i} - \mathscr{R}_{j,i}^{P} \right)^2}{\sum_{i=1}^{q} \left(\mathscr{R}_{j,i}^{P} \right)^2} \right]^2 \tag{1}$$

here, j denotes the Cartesian component of the secondary magnetic field, the index i labels the survey station, $\mathscr{R}$ is the anomalous observed field (defined below), $\mathscr{R}^P$ is the calculated anomalous field, and there are q stations in the survey. The negative sign is included to make the optimization problem a minimization.

A calculated total field $\boldsymbol{R^P} = [R_x^P, R_y^P, R_z^P]$, representing the geometrical (time-independent) part of the electromagnetic response of the dipole, reads:

$$\boldsymbol{R^P} = \alpha\boldsymbol{X} + \beta\boldsymbol{Y} + \gamma\boldsymbol{Z} + \delta\chi^{xy} + \varepsilon\chi^{xz} + \zeta\chi^{yz} + \sum_{j=x,y,z} \left(\lambda_j\boldsymbol{C_j} + \mu_j\boldsymbol{L_j} \right), \tag{2}$$

where the j index labels the Cartesian component of the field and $\alpha, \beta, \gamma, \delta, \varepsilon, \zeta, \{\lambda_j, \mu_j\}$ are weighting coefficients to be determined. The $\boldsymbol{X}$, $\boldsymbol{Y}, \boldsymbol{Z}$ are three-dimensional secondary magnetic fields that account for coupling of an x, y, or z directed magnetic dipole located at the target
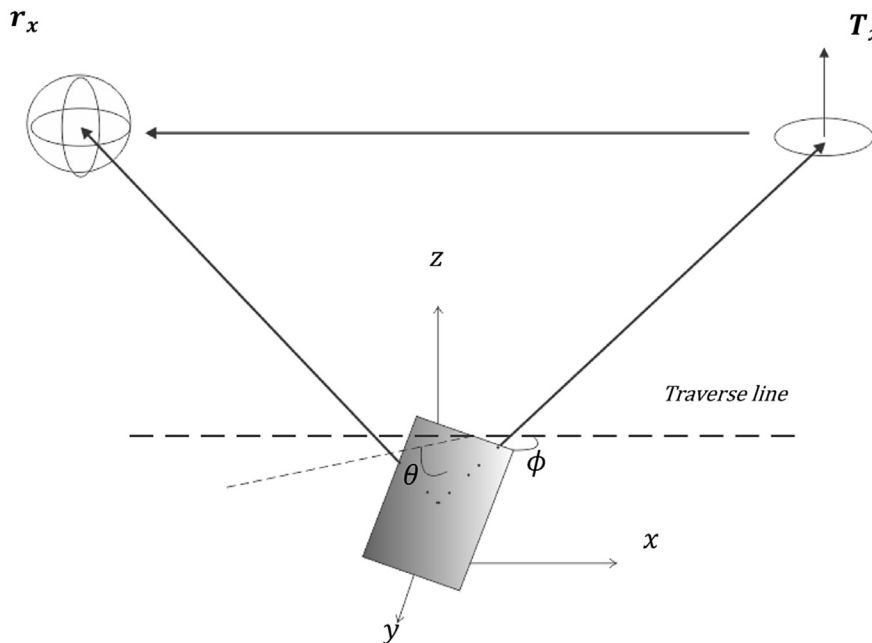

Fig. 1. Schematic diagram of the model under consideration. A dipole conductor is oriented at a strike ϕ in degrees clockwise from the traverse line and a dip θ in degrees below the horizontal. The three-component receiver coil is denoted by $\boldsymbol{r_x}$ and the vertical dipole transmitter by $\boldsymbol{T_x}$.

with an x, y, or z directed primary magnetic field. The χ^{ij} account for coupling of i and j directed magnetic dipoles at the target with i and j directed magnetic fields. Here, the C_j and the L_j account for local and regional background effects in component j of the measurement, respectively. Local background effects preclude the identification of measurements below a threshold value and are therefore represented by constant vectors. Regional background effects have long wavelength responses that appear linear on the scale of an anomaly. They are therefore represented as linear terms. Exact expressions for all the above bold quantities can be found in Desmarais and Smith (2015b). They are stored in vectors of the form $\boldsymbol{B} = [\boldsymbol{B_x}, \boldsymbol{B_y}, \boldsymbol{B_z}]^T$, where $\boldsymbol{B_j}$ are row-vectors of length q for a q-station survey. Because equation (2) represents a time-independent response, the measured data $\boldsymbol{R}$ should be chosen as the field acquired at the window with the highest signal-to-noise ratio.

The weighting coefficients of equation (2) are extracted from the measured data through a least-squares inversion (Desmarais and Smith, 2015b):

$$[\alpha, \beta, \gamma, \delta, \varepsilon, \zeta, \lambda_x, \lambda_y, \lambda_z, \mu_x, \mu_y, \mu_z]^T = \boldsymbol{A}^{\dagger}\boldsymbol{d}, \tag{3}$$

in which T is the transposition operator, $\boldsymbol{A}$ is a linear forward operator, $\dagger$ denotes the generalized inverse, and $\boldsymbol{d}$ is a column-vector function of the measured data.

Once the linear system has been solved, an anomalous (background subtracted) measured data $\mathscr{R}_{j,i}$ is calculated for each j component and i station and used as input to the objective function of equation (1) (Desmarais and Smith, 2015b):

$$\mathscr{R}_{j,i} = R_{j,i} - \lambda_j C_{j,i} - \mu_j L_{j,i}. \tag{4}$$

The objective function compares the anomalous measured data to an anomalous calculated data defined as (Desmarais and Smith, 2015b):

$$\mathscr{R}_{j,i}^P = X_{j,i} + Y_{j,i} + Z_{j,i} + \chi_{j,i}^{xy} + \chi_{j,i}^{xz} + \chi_{j,i}^{yz}. \tag{5}$$

The algorithm also includes normalization as well as windowing along traverse line width determination procedures that we do not repeat here.

The least-squares inversion is necessary because it allows us to determine the amount of background required for modeling the observed data for a pre-specified set of model parameters (location, depth, and orientation of the dipole). To find the set of parameters that best describe the measured data, Desmarais and Smith (2015b) calculate the objective function over a region of parameter space and subsequently find the minimum as the lowest value sampled. Here, we optimize the objective function using serial as well as parallel sampling and PSO. More details follow in the next sections.

2.2. Particle swarm optimization

In the context of the PSO method, the search space is *a priori* defined as (Fernández-Martínez et al., 2010):

$$\boldsymbol{l} \leq \boldsymbol{x}_i(k) \leq \boldsymbol{u}, \quad 1 \leq i \leq d, \tag{6}$$

where k is the iteration number and d is the number of parameters being fitted. Each model parameter i has an associated position $\boldsymbol{x}_i(k)$, which is bounded by lower and upper limits $\boldsymbol{l}_i$ and $\boldsymbol{u}_i$, respectively. At the iteration $k+1$, the algorithm updates the positions and velocities of the particles as follows (Fernández-Martínez et al., 2010):

$$\boldsymbol{v}_i(k+1) = \boldsymbol{\omega} \circ \boldsymbol{v}_i(k) + \phi_1 \circ (\boldsymbol{g}(k) - \boldsymbol{x}_i(k)) + \phi_2 \circ (\boldsymbol{p}_i(k) - \boldsymbol{x}_i(k)) \tag{7}$$

$$\boldsymbol{x}_i(k+1) = \boldsymbol{x}_i(k) + \boldsymbol{v}_i(k+1) \tag{8}$$

$$\phi_1 = r_1 \boldsymbol{a}_g, \quad \phi_2 = r_2 \boldsymbol{a}_p, \tag{9}$$

where $\boldsymbol{v}_i(k)$ is the pseudo-velocity vector of the particle. The $\boldsymbol{a}_g$, $\boldsymbol{a}_p$ are empirically determined vectors of parameters, $(r_1, r_2) \in [0,1] \times [0,1]$ are random numbers (Fernández-Martínez et al., 2010). The $\circ$ denotes the Hadamard (or element-wise) product. These equations are written in vectorial form because the positions and velocities are updated from the values obtained at several previous steps. Here, we evolve the particles at step $k+1$ using the k and $k-1$ dependent weights $\boldsymbol{\omega} = [\omega_{k-1}, \omega_k] = [0.9, 0.4]$, $\boldsymbol{a}_g = [a_{g,k-1}, a_{g,k}] = [0.5, 2.5]$, $\boldsymbol{a}_p = [a_{p,k-1}, a_{p,k}] = [2.5, 0.5]$, as was determined by Voss (2016) through extensive testing on a variety of test functions. For our purposes, experiments (shown below) lead to very satisfactory results. The algorithm is initialized stochastically from a set of potential solutions $\{\boldsymbol{x}_i(0), \boldsymbol{v}_i(0)\}$. For each potential solution, the misfit function I of equation (1) is evaluated. Local and global bests $\boldsymbol{p}_i(k)$, $\boldsymbol{g}(k)$ are then calculated. The local bests are the positions of the lowest misfit for each particle. The global best is the position of the lowest misfit found for the ensemble of particles. This procedure is repeated at each iteration.

Our parallel implementation of the PSO algorithm maps groups (or sub-swarms) of particles to individual processors using the *Message Passing Interface* (*MPI*) libraries. Each particle evolves independently on its processor at iteration k and obtains a set of local minima $\{I_{1:w}(k)\}$ with positions $\{\boldsymbol{p}_{1:w}(k)\}$, if there are w particles on each processor. The global best $\boldsymbol{g}(k)$ is then determined as the position of the smallest $\{I_{1:m}(k)\}$, where m is the number of total particles. The $\boldsymbol{g}(k)$ is then broadcasted to all processors. This scheme is depicted in Fig. 2 and largely follows the approach of Schutte et al. (2004). However, in contrast to Schutte et al. (2004), here we allow processors to evolve sub-swarms independently for $n > 1$ iterations because in practice the overhead associated with communication of the processors can exceed the benefits of updating $\boldsymbol{g}(k)$ at each iteration. In this manner, parallelization of the PSO approach is optimized according to machine architecture and massive parallelization can be achieved in heterogeneous architectures by allowing processors with variable interconnects to communicate at variable rates. In principle, the fact that the global best $\boldsymbol{g}(k)$ is broadcasted every $n > 1$ iterations affects the particle trajectories and rate of convergence. However, these are only slightly disturbed, provided that n is sufficiently small. Experimentation has shown that negligible idle time occurs at barriers while synchronizing the processors because computation time is highly similar on all processors. We therefore adopt a barrier-containing scheme rather than an asynchronous scheme, in which the global best would be dynamically shared amongst processors As described in the introduction, other PSO variations have been proposed, each of which are characterized by different stability regions and convergence rates. However, for our purposes, we obtain satisfactory performance using the basic algorithm and hence restrict ourselves to this approach. A complete study on the effect of the PSO variant on the performance of the algorithm could be the focus of a future study.

3. Results

3.1. Synthetic models

For the purposes of testing the various optimization procedures, we first experiment on a synthetic model. The simulated electromagnetic survey consisted of a dipole transmitter placed at a height of 120 m above ground with a dipole moment of 2.2E06 A m^2 in the vertical direction. A tri-axial receiver was towed 50 m below and 128 m behind the transmitter. This transmitter-receiver geometry coincides with the MEGATEM and GEOTEM system geometries (Desmarais and Smith, 2015d). A dipole conductor was placed at a 1 m offset to the transmitter-receiver system and placed at the center of the traverse line. The depth of the conductor was 100 m, its strike (azimuthal angle from traverse line) was 30°, and its dip (inclination angle from horizontal) was 80° (The strike and dip orientations are further explained in Fig. 1 and its caption). The 1 m offset and intermediate strike and dip angles were chosen to avoid
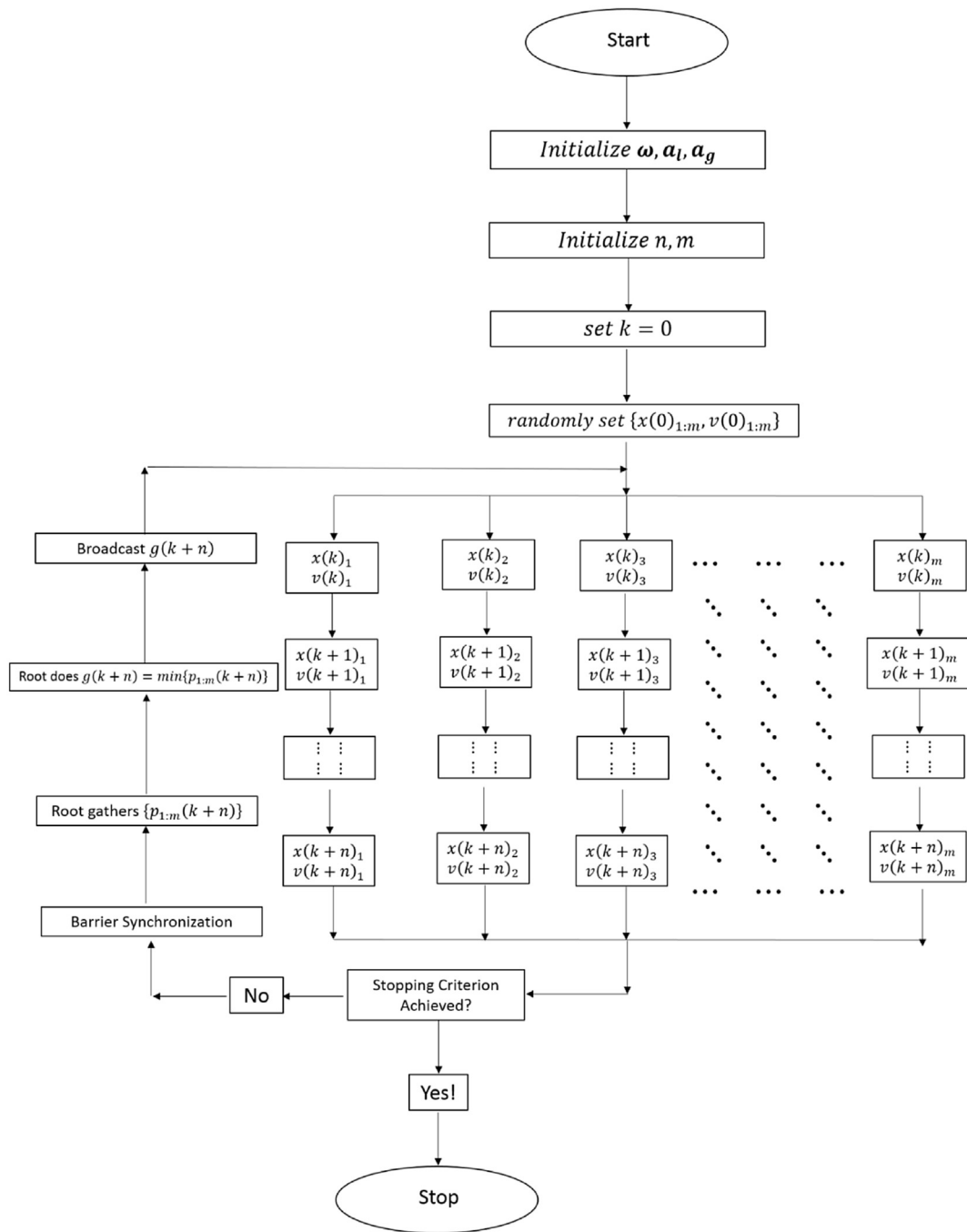
Fig. 2. Schematic diagram depicting the flow of the parallelized PSO implementation; m denotes the number of particles, and n denotes the communication rate of the processors. To simplify the figure, we assume that there is one particle per processor and that all the processors communicate at the same rate.

null-coupling of the y-component of the measurement because the lack of this component inhibits uniaxial transmitter systems from resolving the correct geometrical parameters (Desmarais and Smith, 2015d). Here, we limit our synthetic tests to this model because Desmarais and Smith (2015d, 2015b) have already shown that the algorithm is always capable of extracting the correct parameters for a uniaxial transmitter (if the y-component of the measurement exists) or a two-axis transmitter (if the y-component of the measurement does not exist). The electromagnetic response of this model can be seen in the solid lines of Fig. 3.

We first discuss the results obtained using the standard sampling minimization procedure. The objective function was sampled for conductor positions of −100 m to 100 m at 10 m intervals along the direction normal and parallel to the traverse line. Here, the origin is the center of the survey. The depth below ground parameter was sampled from 0 m to 500 m at 25 m intervals. The strike and dip parameters were sampled from 0° to 180° and 90° at 10° and 5° intervals, respectively. Fig. 4 shows the wall-clock times obtained after running a *MATLAB* code on several cores of the *zeno* cluster at the University of Saskatchewan that has eight computational nodes consisting of two six-CPU Intel Xeon E5649 2.53 GHz multi-core processors and four Infiniband interconnects. The code was parallelized through domain decomposition using the *MATLAB parfor* construct, which parallelizes the *for* loops using an approximate block partition. Each processor evaluated the objective function within a subset of the search-space. After all of the evaluations were performed, all values of the objective function were imported to the root processor, which located the minimum of I and returned the position
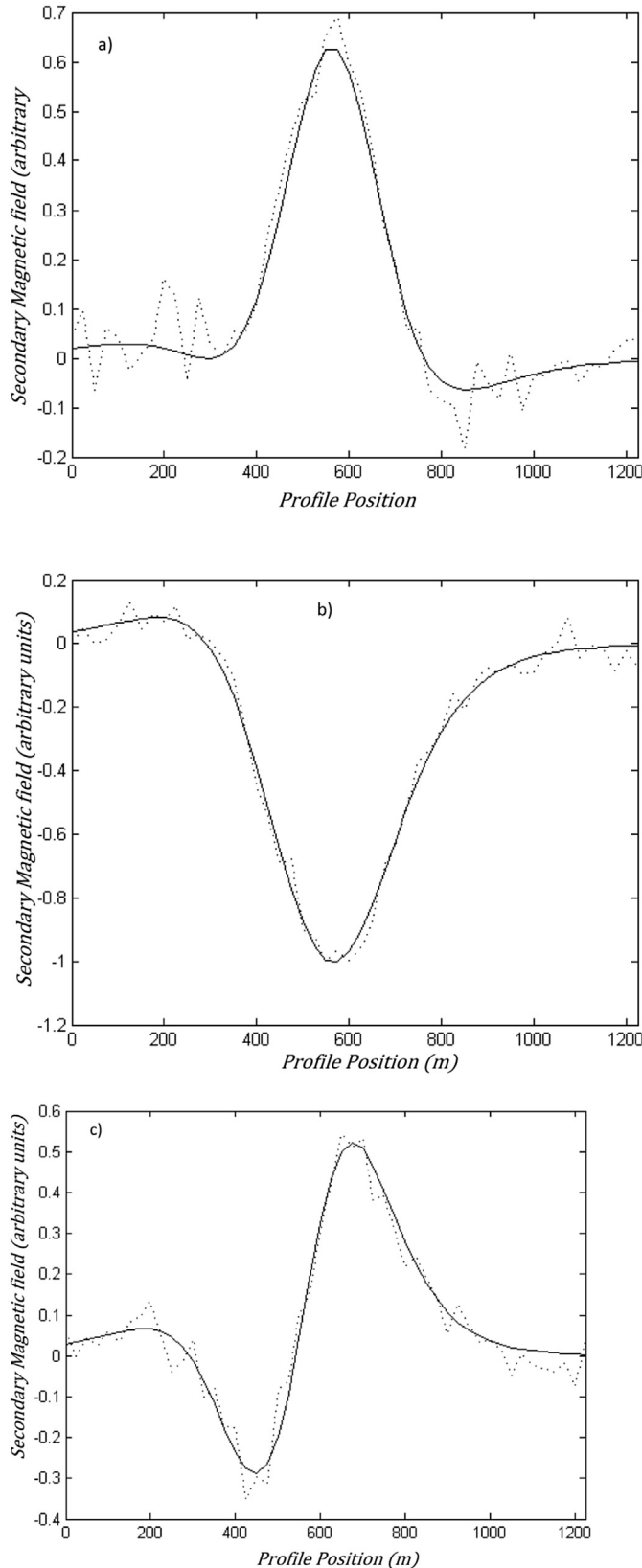
Fig. 4. Wall-clock times obtained using the standard sampling *MATLAB* code.

Fig. 3. (a) *x*-component (b) *y*-component, and (c) *z*-component of the secondary magnetic field of the synthetic model under consideration. The dotted line represents the signal augmented with random Gaussian noise at a signal-to-noise ratio of 25.
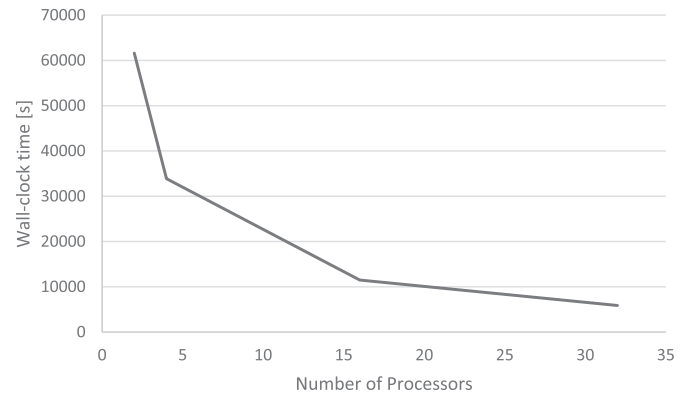
of this minimum. In all cases, the global minimum of the objective function was found, and the correct parameters were predicted (with exception to the offset from the traverse line, which was of course off by 1 m). The wall-clock times are on the order of thousands of seconds, so that it takes a few hours to locate the minimum of the objective function using this approach.

The PSO algorithm calculated the objective function using a *MATLAB* code and a PSO script written in *Python*. We parallelized the PSO algorithm using the *mpi4py* libraries, which contains the equivalent of many *MPI* functions for the *Python* programming language. Ideally, the processors would share the local bests and find the global best with a call to the *MPI allreduce* function, using the *MPI_MINLOC* reduction operator. Such a call would simultaneously broadcast all local bests to the entire communicator as well as find the global best and the processor on which the global best resides. However, this operator is not implemented in the *mpi4py* package at the time of this publication. Instead of calling *allreduce*, we proceed as follows. The root processor gathers the local bests using a call to *allgather* (from which all processors obtain all of the local bests), the global best and "best" processor (i.e., the processor on which the global best resides) is then determined using the *Python* function *min* (which is a function that finds the minimum of elements in a list (values of objective functions associated with global best), as well as the index of this element in the list (best processor)); these values are subsequently broadcasted to the rest of the communicator. In any case, it turns out that the total time associated with communication of the processors is small compared to the evaluations of the objective function so that the extra time for performing these operations is not crucial to our evaluation of the wall-clock time. It is also worth mentioning that results obtained for communication times of the processors are mostly independent on whether or not a lower-level programming language was used because processor communication times are dominantly driven by the processor interconnect.

We defined the stopping criterion as $I < -0.9999$ (for the synthetic model) or that the value of I associated with $g(k)$ remains constant for 100 iterations (for the Chibougamau field example, see below). The threshold on I guaranteed that the position of the minimum was within $1 - 2$ m and $1 - 2°$ of the correct values. Experimentation has shown that good results are obtained using 70 particles. The computations were performed using the same grid boundaries as in the uniform sampling code.

We ran the PSO algorithm several times on 1 to 6 cores (within the same node) of the *zeno* cluster at the University of Saskatchewan. Fig. 5 shows the wall-clock times obtained when using a communication rate of $n = 1$; i.e., the frequency, in terms of the number of iterations, at which information about the global best is exchanged between processors. The fact that variable wall-clock times are obtained for constant communicator size occurs because of the stochastic nature of the PSO method (r_1, r_2 are random numbers, and $x_i(k)$, $v_i(k)$ are randomly initialized). So the variability of the results in Fig. 5 are mostly due to the fact that the
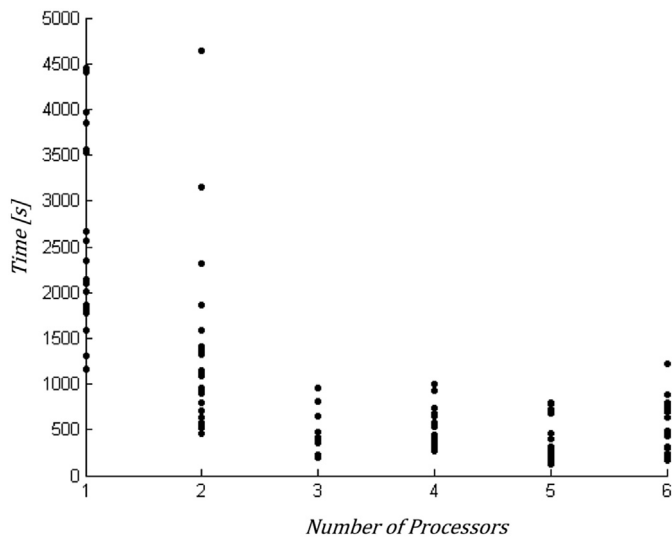
Fig. 5. Wall-clock times obtained for the PSO algorithm using a communication rate of $n = 1$. Various times are obtained for constant communicator size because of the stochastic nature of the PSO algorithm. The wall-clock time is optimized using ~ 3 processors. Wall-clock times are obtained down to 100 s, so that the time to run the code has been improved by two orders of magnitude when compared to the sampling code.

PSO algorithm can take variable iterations to converge and are not related to the communication rate. Even though the results are highly variable, with a sufficiently large sample of run-times like in Fig. 5, we can safely say that the wall-clock time is optimized using ~ 3 processors. Wall-clock times are obtained down to 100 s, implying that the time to run the code has been improved by two orders of magnitude compared to the direct sampling code. For the purposes of increasing the scalability of the code, we subsequently ran it using 6 processors and varied the communication rate. The results are shown in Fig. 6. As can be seen from this figure, the wall-clock time of PSO depends weakly on the communication rate, at least for the objective function under consideration and the chosen system architecture. This occurs because the cost associated with evaluating the objective function greatly outweighs the overhead associated with processor communication.

3.2. Sensitivity analysis of the solution

For the purposes of performing a basic sensitivity analysis of the solution, we have added random Gaussian noise to the electromagnetic response of the dipole conductor. The noise-added response is displayed

in the dotted lines of Fig. 3. The noise was added using discrete Gaussian functions, whose absolute amplitudes did not exceed one twenty-fifth of the absolute amplitude of the relevant Cartesian component of the secondary magnetic field response (signal-to-noise ratio (SNR) of 25, mean zero, and standard deviation of unity). This SNR was chosen high enough to be representative of what would be encountered in a noisy AEM survey, yet low enough that the overall shape of the response is still preserved, so that it is still possible to resolve the geometrical parameters of the target. We plot the evolution of $\boldsymbol{g}(k)$ and of the associated values of I for representative simulations in Fig. 7(a–e) for the noise-free and noise-added cases. The inserts in Fig. 7(a–e) are close-ups for the first 300 iterations.

We can make two observations based on from Fig. 7(a–e). First, it is evident that the noise causes only a slight shift of the position of the global minimum. This can be observed from the fact that the final values of the various geometrical parameters are different in the dotted (noisy) and solid (noise-free) lines. The largest discrepancy between the noise-added and noise-free parameters is an overestimate of the depth below surface by ~ 10 m in the noise-added case. We ran the noisy simulations ten times and obtained a position along the traverse line of -0.84 m to -3.33 m; an offset from the traverse line of -1.28 m to -1.43 m; a depth below surface of 111.10 m–105.42 m; a dip of $31.79°$ to $32.06°$; a strike of $79.94°$ to $86.69°$. We view these discrepancies as within reasonable error bounds for most AEM applications. The full sets of parameters are presented in Table 2.

The second observation that can be made from Fig. 7(a–e) is that the trajectories in the noisy simulation converge to the global minimum more quickly, whereas the trajectories in the noise-free simulation are initially more explorative (see inserts in Fig. 7(a–e)) and take longer to relax to the global minimum. This difference may be because exploration of the trajectories is more restricted by the more jagged topography of the objective function in the noisy simulation. This is also a manifestation of the fact that noise can speedup the convergence to equilibrium in a stochastic process.

3.3. Test at the Chibougamau site, Québec

To show some practical capabilities of the new algorithm, we have tested the PSO code for interpreting a MEGATEM AEM survey conducted at the Chibougamau site in Québec. This is the same survey discussed by Desmarais and Smith (2015b, c, d). The decreased wall-clock time yielded by the PSO method means that we were able to easily interpret this survey along all 7 traverse lines instead of only one line as was done in previous work (Desmarais and Smith, 2015b, c, d). A plan view of the survey configuration with a contour map of the T-component (or total
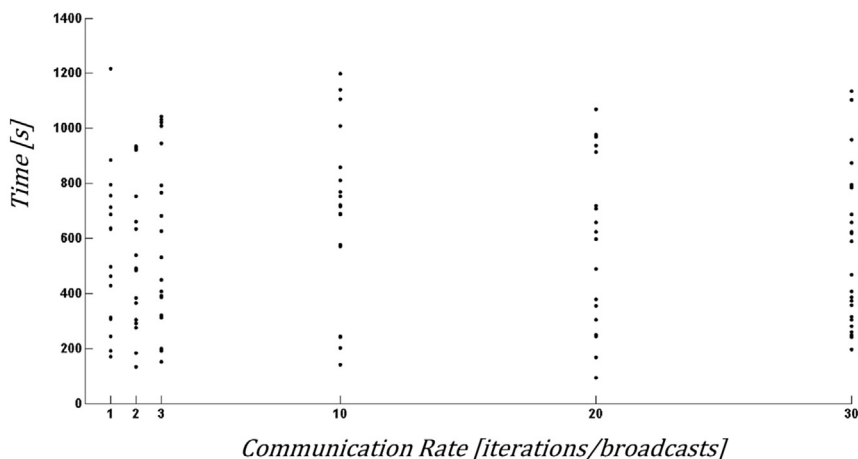

Fig. 6. Wall-clock times while varying the communication rate with 6 processors. The plot shows that the wall-clock depends weakly on the communication rate.
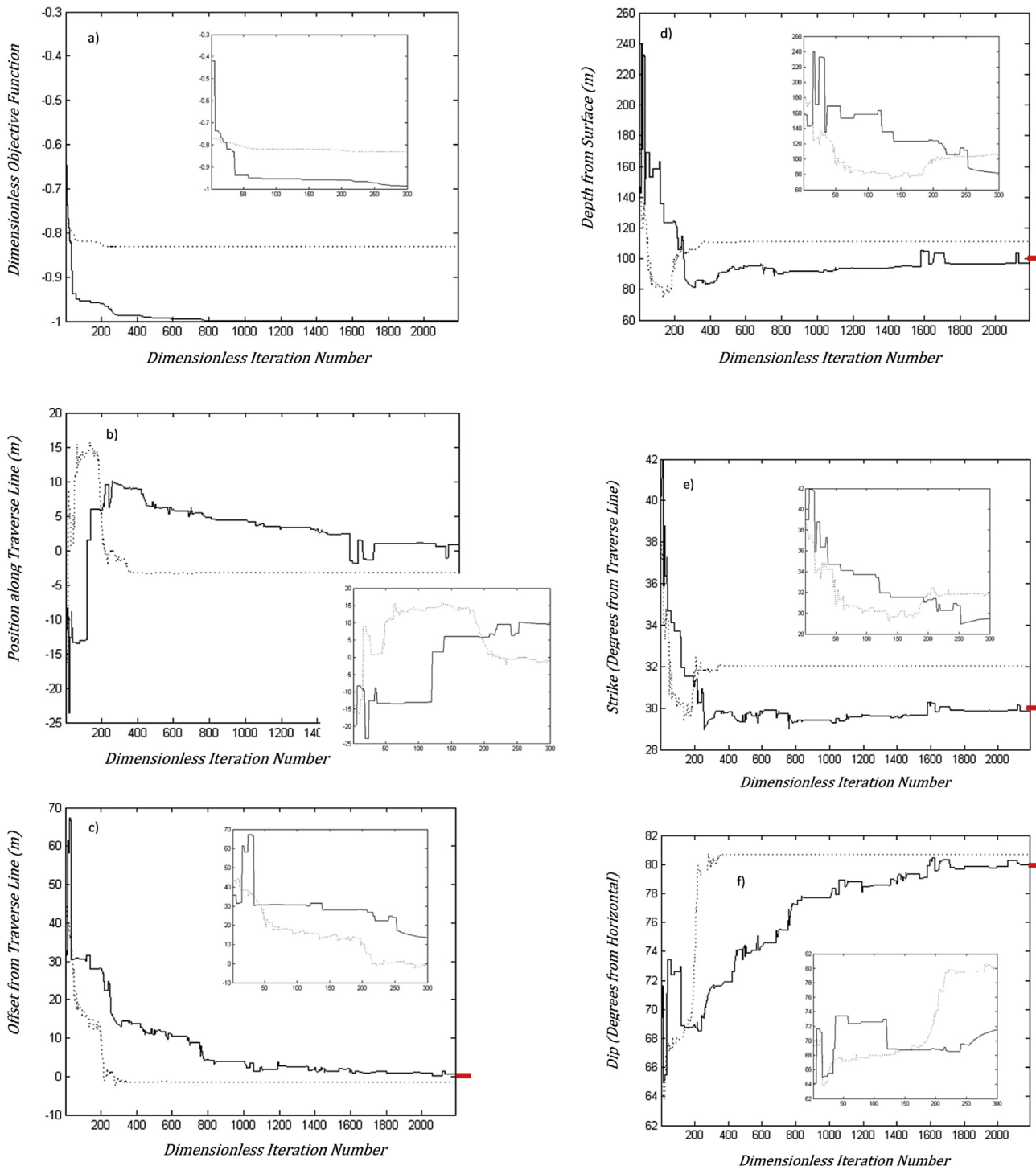
Fig. 7. PSO trajectories for the noisy cases (dotted line) and noise-free (solid line) (a) objective function (b) position along the traverse line (c) offset from the traverse line (d) depth from the surface (e) dip angle (f) strike angle. The inserts in the figures are close-ups for the first 300 iterations. The red rectangle at the right of the figures b–f indicate the target values. (For interpretation of the references to colour in this figure legend, the reader is referred to the web version of this article.)

field) of the electromagnetic response is presented in Fig. 8. The T-component has been plotted because it can be used as a rough measure of strike and location of the conductor (Desmarais and Smith, 2015c). The geometrical parameters extracted from the PSO approach are presented in Table 1. Here, the position along the traverse line is found to vary from line to line because the conductor is oriented at an angle to the traverse line ($0° <$ strike $< 180°$) and because the traverse lines are not parallel to each other (see Fig. 8). We also include the value of the objective function

I obtained from the fitting. In principle, if the fit is perfect, then I has a value of -1. Higher (i.e., more positive) values indicate imperfect fits. There are two reasons for the obtained imperfect fits. First, our theory represents the conductor as a magnetic dipole; this assumes that the dimensions of the conductor are small when compared to the distance from the conductor to the transmitter-receiver system. This approximation may not be ideal if the portion of the charge distribution located in the vicinity the traverse line is delocalized. Second, the present approach
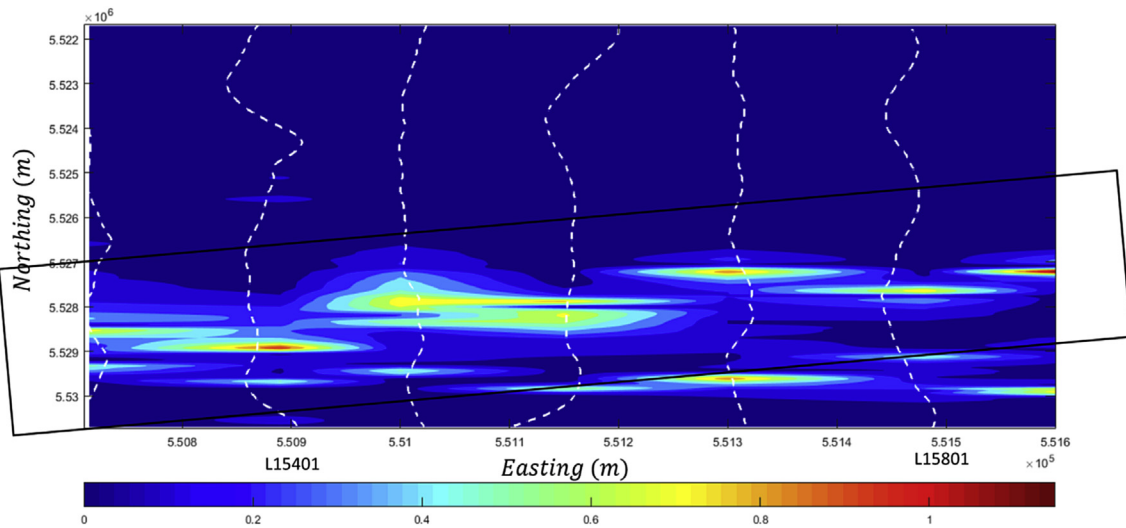
Fig. 8. The T-component (or vector magnitude) of the measured secondary magnetic-field response at the Chibougamau test site. The black dashed line shows the location of the traverse lines, which are labelled at the bottom of the figure. The units of the plotted magnetic field are arbitrary. The boxed feature was interpreted.

Table 1
Geometrical parameters obtained at the Chibougamau site. In the last row, parameters are provided from previous studies for line 15701. The first number is that obtained from Desmarais and Smith (2015b,d) and the second number is from Desmarais and Smith (2015c). Desmarais and Smith (2015b,d) also evaluate the same objective function (albeit using a different optimization procedure), and the value of the objective function for the relevant parameters is presented in the last element of the table.

Line Number	Position Along Traverse Line [m]	Offset From Traverse Line [m]	Depth Below Surface [m]	Dip (inclination angle from horizontal) [°]	Strike (azimuthal angle from traverse line) [°]	Objective Function [unitless]
L15301	6848	23.4	188	85.0	65.0	−0.70717
L15401	6971	0.86	115	68.3	93.7	−0.73877
L15501	6816	5.37	100	3.5	26.7	−0.37082
L15601	5595	7.44	137	65.0	142.3	−0.74230
L15701	5404	11.3	187	80.8	67.5	−0.86307
L15801	5316	3.69	151	73.7	126	−0.65503
L15901	5155	13.2	120	76.9	73.9	−0.59321
L15701	5555, 5480	0.00, 0.00	175, 130	80.0, 82.5	65.0, 75.0	−0.83470

Table 2
Full sets of parameters obtained for the 10 noise-added synthetic models.

	Position Along Traverse Line [m]	Offset From Traverse Line [m]	Depth Below Surface [m]	Dip (inclination angle from horizontal) [°]	Strike (azimuthal angle from traverse line) [°]	Objective Function [unitless]
1	−0.84	−0.65	105.42	31.79	79.94	−0.831080
2	−3.26	−1.42	110.98	32.03	80.70	−0.831349
3	−3.26	−1.42	111.01	32.03	80.69	−0.831349
4	−3.33	−1.29	111.06	32.06	80.66	−0.831345
5	−3.28	−1.39	111.10	32.03	80.68	−0.831348
6	−3.26	−1.42	110.99	32.03	80.69	−0.831349
7	−3.25	−1.40	110.99	32.06	80.68	−0.831344
8	−3.25	−1.43	110.94	32.02	80.70	−0.831349
9	−3.25	−1.41	110.98	32.03	80.69	−0.831349
10	−3.25	−1.41	110.98	32.03	80.69	−0.831349

does not provide a formal theory for describing the interaction between the dipole and background because we simply supply a means to subtract background terms from the total response (see equation (4)). Visual inspection of the raw data has shown that higher values of I (worse fits) are obtained along the traverse lines for which the response includes significant interaction between the conductor and the background (Lines L15501, L15601, L15801). This is made evident in Fig. 9, where the measured responses are plotted alongside the fitted responses for all components and along all traverse lines. However, the decreased wall-clock time afforded by the parallel PSO approach opens the possibility for calculating electromagnetic responses using a higher level of approximation, such as interaction with an overlying conductive thin horizontal sheet, e.g., using the formula of Desmarais and Smith (2016).

As such, formal account of interaction between the conductor and background now appears as a viable alternative for future work. This could be done so that better results could be obtained along lines L15501, L15601, and L15801.

The conductor responsible for the studied anomaly has important strike length (as made evident in Fig. 8). As well, as can be seen in the available geological map of the area (Paradis, 2010), geological strata have orientations that become increasingly parallel to the strike of the conductor as a function of distance from the conductor. This supports an interpretation that the conductor represents a structural feature, such as a fault, which postdates the age of the surrounding strata. A more detailed interpretation would require more specific geological and geophysical data.
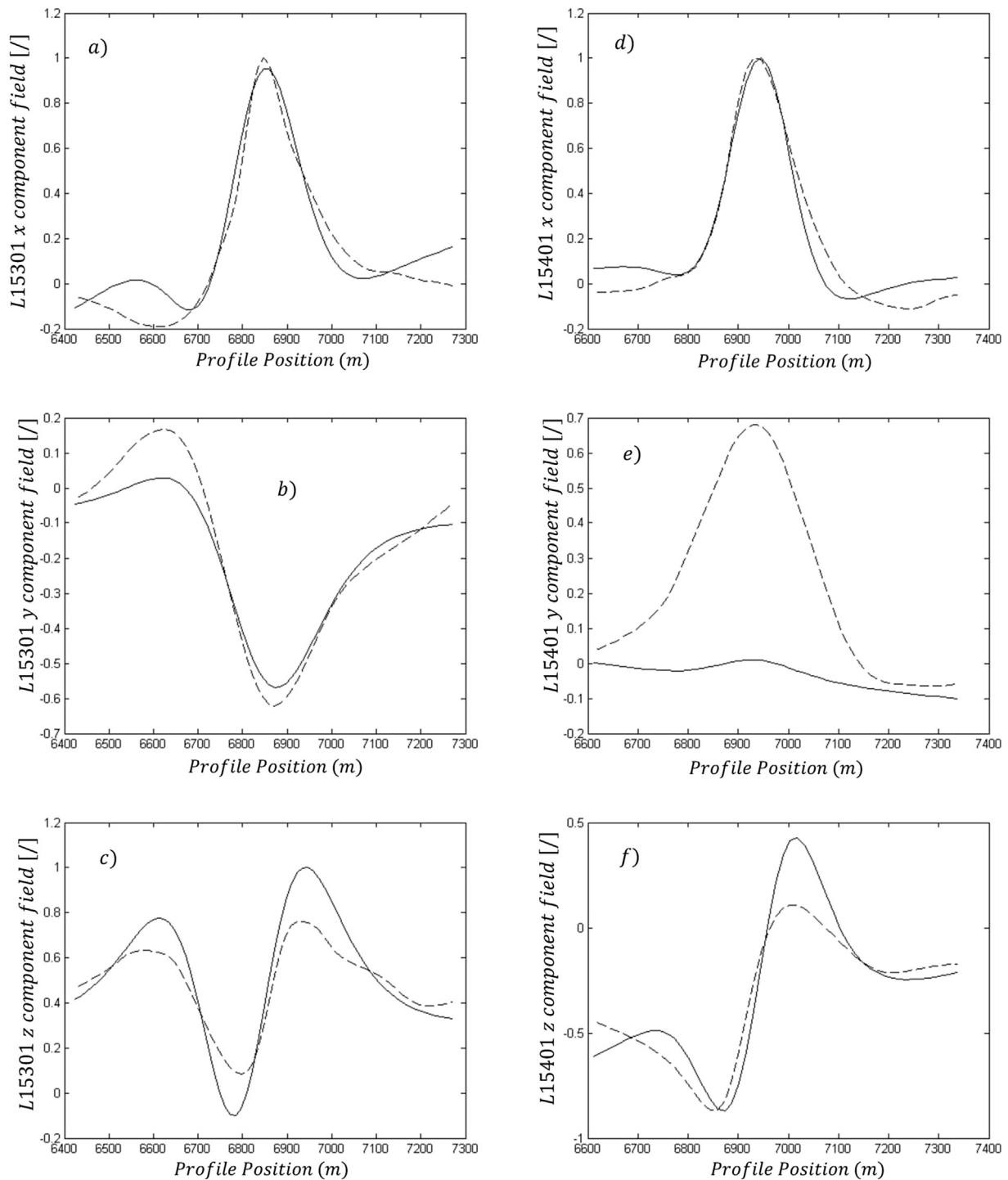
Fig. 9. a) *x*, b) *y*, c) and *z* components of the secondary magnetic field along line 15301. The measured response is in the dashed line and the synthetic response is in the solid line. The other figures are similar but for the other lines of the survey: d), e), f) are for line 15401; g), h), i) are for line 15501; j), k), l) are for line 15601; m), n), o) are for line 15701; p), q), r) are for line 15801; s), t), u) are for line 15901. It can be seen in figures g), h), i), j), k), l) and p), q), r) that the field is broadened by a long wavelength response, caused by background effects that are not represented in our model. These effects are especially serious in the case of figures j), k), l) (line 15501). However, good fits are obtained along other lines. In all of these figures, the magnitude of the field has arbitrary units.

4. Conclusion

Interpretation of airborne electromagnetic data can be achieved in a quick and efficient manner using our parallelized implementation of the particle swarm optimization algorithm. The interpretation is performed by minimizing an objective function that evaluates the least-squares difference between the measured data and a set of synthetic data, calculated using a time-independent dipole conductor formula. When tested on a synthetic model, we find that for the chosen system architecture and objective function, the particle swarm optimization algorithm depends weakly on the communication rate of the processors. We also find that wall-clock times are improved by two orders of magnitude
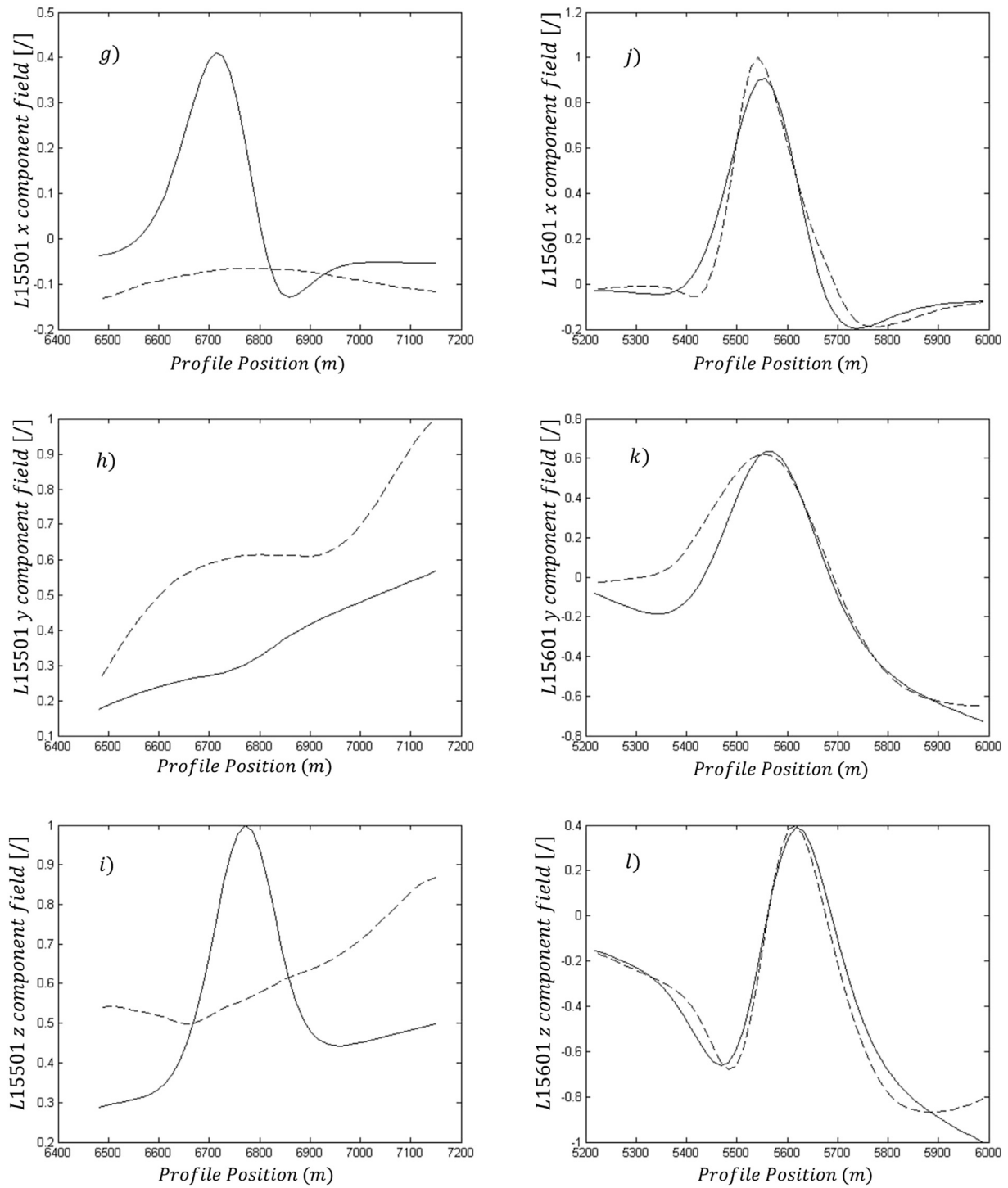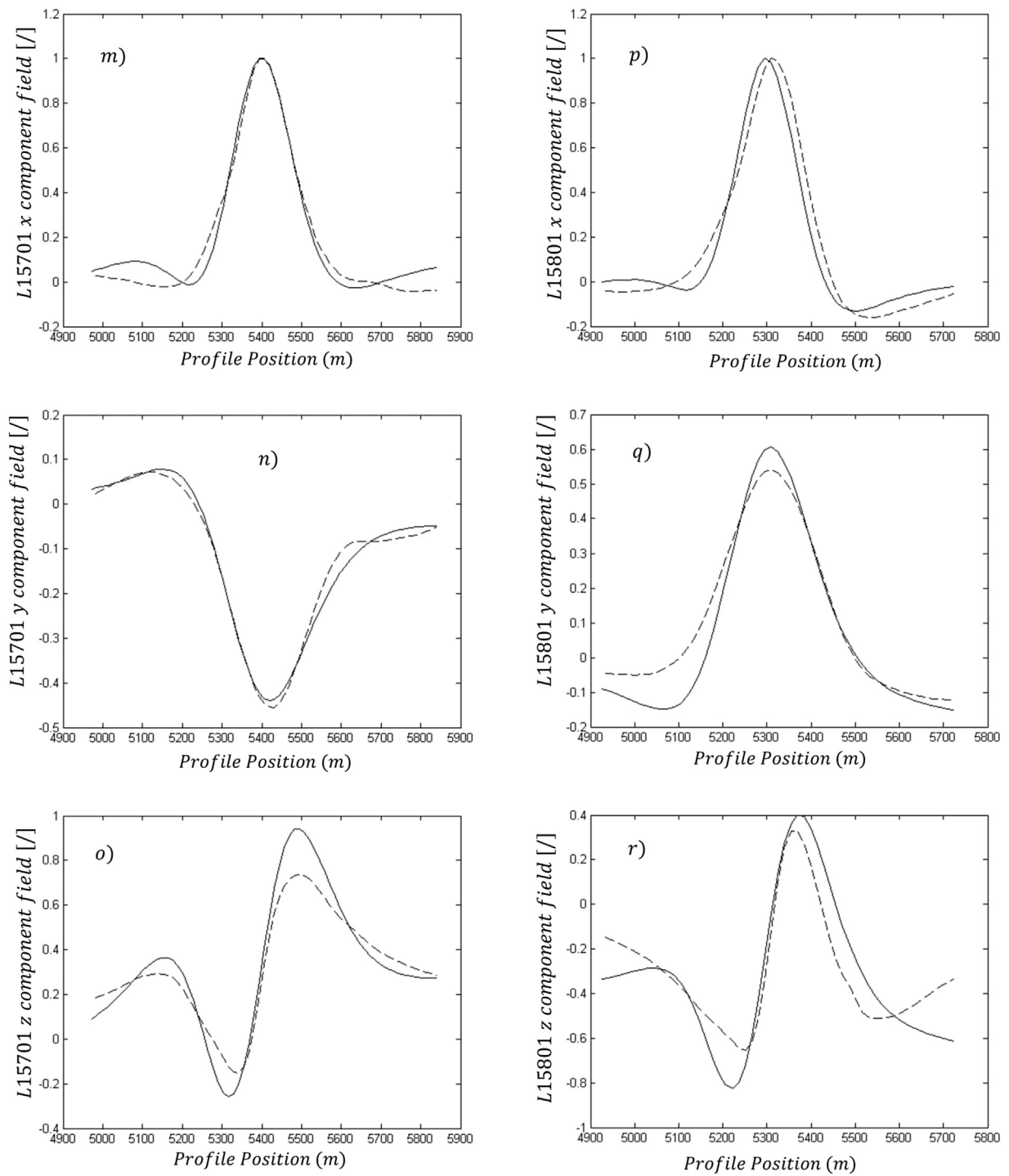
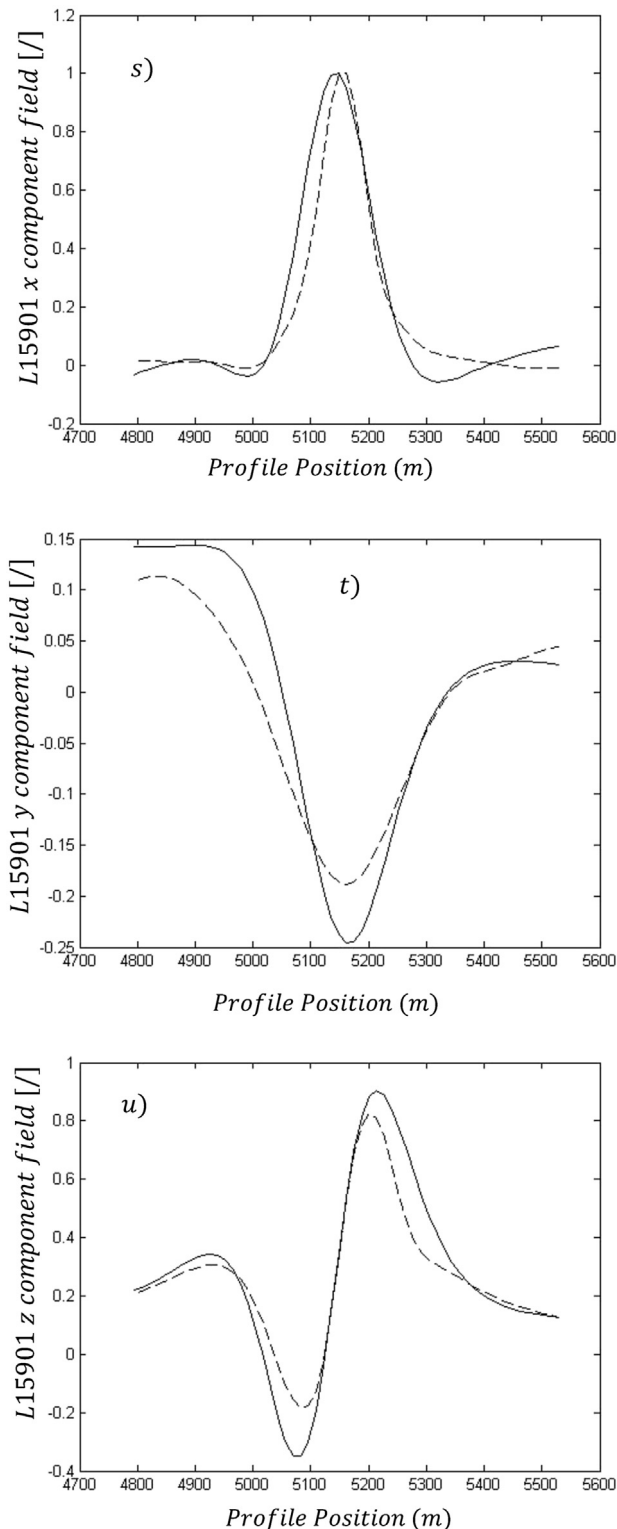Fig. 9 (continued).

Fig. 9 (*continued*).

Fig. 9 (*continued*).

when compared to the minimization procedure of Desmarais and Smith (2015a). As such, airborne surveys of several anomalies can now be easily interpreted, as was shown from a test at the Chibougamau site. The improved efficiency of the algorithm also opens the possibility of including a higher level of approximation.

References

Cheng, J.L., Fei, P., Suping, S., Xiaoyun, J., Zheng, Jia, J., 2015. Joint inversion of TEM and DC in roadway advanced detection based on particle swarm optimization. J. Appl. Geophys. 123, 30–35.

Desmarais, J.K., Smith, R.S., 2015a. Survey design to maximize the volume of exploration of the InfiniTEM system when looking for discrete targets. J. Appl. Geophys. 115, 11–23.

Desmarais, J.K., Smith, R.S., 2015b. Decomposing the electromagnetic response of magnetic dipoles to determine the geometrical parameters of a dipole conductor. Explor. Geophys. 47, 13–23.

Desmarais, J.K., Smith, R.S., 2015c. The total component (or vector magnitude) and the energy envelope as tools to interpret airborne electromagnetic data: a comparative study. J. Appl. Geophys. 121, 116–127.

Desmarais, J.K., Smith, R.S., 2015d. The benefits of using multicomponent-transmitter-receiver systems for determining the geometrical parameters of a dipole conductor. Explor. Geophys. 47, 1–13.

Desmarais, J.K., Smith, R.S., 2016. Approximate semi-analytical expressions for the electromagnetic response of a sphere interaction with conductive overburden. Geophysics 81, E265–E277.

Dyck, A.V., West, G.F., 1984. The role of simple computer models in interpretations of wide-band, drillhole electromagnetic surveys in mineral exploration. Geophysics 49, 957–980. http://dx.doi.org/10.1190/1.1441741.

Dyck, A.V., Bloore, M., Vallée, M.A., 1981. User Manual for Programs PLATE and SPHERE: Research in Applied Geophysics, 14, Geophysics Laboratory Department of Physics. University of Toronto.

Fernández-Álvarez, J.P., Fernández-Martínez, J.L., García-Gonzalo, E., Menéndez-Pérez, C.O., 2006. Application of the Particle Swarm Optimization Algorithm to the Solution and Appraisal of the Vertical Electrical Sounding Inverse Problem. International Association of Mathematical Geology (IAMG06, Liège. September 2006.

Fernández-Álvarez, J.P., Fernández-Martínez, J.L., Menéndez-Pérez, C.O., 2008. Feasibility analysis of the use of binary genetic algorithms as importance samplers application to a geoelectrical VES inverse problem. Math. Geosci. 40 (34), 375–408.

Fernández-Martínez, J.L., García-Gonzalo, E., 2009. The PSO family: deduction, stochastic analysis and comparison. Swarm Intell. 3, 245–273.

Fernández Martínez, J.L., García Gonzalo, E., 2011. Stochastic stability analysis of the linear continuous and discrete PSO models. IEEE Trans. Evol. Comput. 15 (3), 405–423.

Fernández Martínez, J.L., Gonzalo, E.G., Fernandez Alvarez, J.P., Kuzma, H.A., Menendez Perez, C.O., 2010. PSO: a powerful algorithm to solve geophysical inverse problems. Application to a 1D-DC resistivity case. J. Appl. Geophys. 71, 13–25.

Fullagar, P.K., Pears, G.A., Reid, J.E., Schaa, R., 2015. Rapid approximate inversion of airborne TEM. Explor. Geophys. http://dx.doi.org/10.1071/EG14046.

Golub, G.H., Pereyra, V., 1973. The Differentiation of pseudo-inverses and nonlinear least squares problems whose variables separate. SIAM J. Numer. Anal. 10 (2), 413–432.

Kennedy, J., Eberhart, R., 1995. Particle swarm optimization. In: Proceedings of the Fourth IEEE International Conference on Neural Networks. IEEE Service Center, Perth, Australia, pp. 1942–1948.

Lamontagne, Y., Macnae, J., Polzer, B., 1988. Multiple conductor modeling using program multiloop. SEG Tech. Program Expand. Abstr. 1988, 237–240. http://dx.doi.org/10.1190/1.1892248.

Macnae, J.C., Smith, R., Polzer, B.D., Lamontagne, Y., Klinkert, P.S., 1991. Conductivity-depth imaging of airborne electromagnetic step-response data. Geophysics 56, 102114.

Macnae, J., King, A., Stolz, N., Osmakoff, A., Blaha, A., 1998. Fast AEM data processing and inversion. Explor. Geophys. 29, 163–169. http://dx.doi.org/10.1071/EG998163.

Macnae, J., 2015. 3D-spectral CDIs: a fast alternative to 3D inversion? Explor. Geophys. 46, 12–18. http://dx.doi.org/10.1071/EG14036.

Naudet, V., Fernández-Martínez, J.L., García-Gonzalo, E., Fernández-Álvarez, J.P., 2008. Estimation of water table from self-potential data using particle swarm optimization (PSO). 2008 Annual Meeting. SEG, Expand. Abstr. 27 (1), 1203–1207.

Pallero, J.L.G., Fernández Martínez, J.L., Bonvalot, S., Fudym, O., 2015. Gravity inversion and uncertainty assessment of basement relief via Particle Swarm Optimization. J. Appl. Geophys. 116, 180–191.

Paradis, S.J., 2010. Surficial geology, Chibougamau, Quebec/Geologie des formations superficielles. Geological Survey of Canada, Chibougamau, Quebec. Open File 6064, scale 1:250 000.

Penrose, R., 1955. A generalized inverse for matrices. Math. Proc. Camb. Philosophical Soc. 51, 406–413.

Pethick, A., Harris, B., 2016. Macro-parallelisation for controlled source electromagnetic applications. J. Appl. Geophys. 124, 91–105.

Reddy, M.J., Kumar, D.N., 2005. Multi objective particle swarm optimization for optimal reservoir operation. In: Proceedings of 2nd Indian International Conference on Artificial Intelligence (IICAI-2005), India, December 20–22, 2005, pp. 1183–1192.

Reid, J., Fitzpatrick, A., Godber, K., 2010. An overview of the SkyTEM airborne EM system with Australian examples. Preview 145, 27–37.

Shaw, R., Srivastava, S., 2007. Particle Swarm Optimization. A new tool to invert geophysical data. Geophysics 72 (2), F75–F83.

Schaa, R., 2010. Rapid Approximate 3D Inversion of TEM Data. University of Tasmania. Ph.D. thesis.

Schutte, J.F., Reinbolt, J.A., Fregly, B.J., Haftka, R.T., George, A.D., 2004. Parallel global optimization with the particle swarm algorithm. Int. J. Numer. Methods Eng. 61, 2296–2315.

Smith, R.S., Chouteau, M.C., 2006. Combining airborne electromagnetic data from alternate flight directions to improve data interpretability: the virtual symmetric array. Geophysics 71, G35–G41. http://dx.doi.org/10.1190/1.2187745.

Smith, R.S., Wasylechko, R., 2012. Sensitivity cross-sections in airborne electromagnetic methods using discrete conductors. Explor. Geophys. 43, 95–103.

Vallée, M.A., 2015. New developments in AEM discrete conductor modelling and inversion. Explor. Geophys. 46, 97–111.

Voss, K., 2016. pythOPT: a Problem-solving Environment for Optimization Methods. Department of Computer Science, University of Saskatchewan. M.Sc. Thesis.

Wolfgram, P., Hyde, M., Thompson, S., 1998. How to find localized conductors in GEOTEM data. Explor. Geophys. 29, 665–670.

Yin, C.C., Ren, X.Y., Liu, Y.H., Qi, Y.F., Qiu, C.K., Cai, J., 2015. Review on airborne EM inverse theory and applications. Geophysics 80, W17–W41.